ILASS Americas 27th Annual Conference on Liquid Atomization and Spray Systems, Raleigh, NC, May 2015

Steady State and Transient, Non-isothermal Modeling of Cavitation in Diesel Fuel Injectors

R. Salemi[*1], R. McDavid[2], P. Koukouvinis[3], M. Gavaises[3], and M. Marengo[4, 5]

[1]Large Power Systems Division
Caterpillar UK Engines Co. Ltd, Peterborough, PE1 5FQ UK
[2]Energy and Transportation Research
Product Development and Global Technology
Caterpillar Inc., Mossville, IL 61552, USA
[3]School of Engineering and Mathematical Sciences,
City University, London EC1V 0HB, UK
[4]School of Computing, Engineering and Mathematics
University of Brighton, Brighton BN2 4GJ, UK
[5]Dept. of Engineering and Applied Sciences,
University of Bergamo, Viale Marconi 5, 24044 Dalmine, Italy

Abstract

This paper describes preliminary results of non-isothermal CFD simulations of both single phase steady state flow at 5µm axial needle lift and two phase cavitating transient flow during a full injection cycle for three different diesel fuel injector designs. The CFD simulations are carried out under typical engine operating boundary conditions with variable fuel injector inlet pressure ranging from about 160 to 190MPa, a constant inlet temperature of 80^oC and a typical constant outlet pressure of 10MPa. The non-isothermal CFD simulations, carried out using the in-house CFD code from City University in London (GFS), employ variable properties for diesel liquid as functions of both pressure and temperature. Additionally, the effects of viscous heating were taken into account in order to further improve the accuracy of the physics of the flow field within such fuel injectors. The paper provides a comparison of the variations of the coefficient of discharge and the temperature rise across each of the fuel injector designs during one full injection cycle. Furthermore the geometrical locations within the fuel injector, where the predicted cavitation might lead to erosion, are examined, while at the same time providing the novelty of outlining the likelihood of the occurrence of the flow boiling under the boundary conditions used.

[*]Corresponding author: Salemi_Ramin@cat.com

Introduction

Although the modern diesel engines requirement of operating at fuel injection pressures of up to 300MPa has placed less demand on the aftertreatment systems in meeting the legislative Tier IV emission requirements, it has made the fuel injection systems more vulnerable to cavitation and boiling phenomena and their consequent erosion damage [1], [2]. Cavitation occurs when the liquid pressure at a given temperature falls below its saturation vapour pressure and as a result a change of phase occurs from liquid to gaseous phase. Furthermore bubbles may arise from flow boiling phenomena when the liquid temperature at a given pressure rises above its saturation temperature.

It is now well known that cavitation formation often leads to the process of violent collapse of gaseous bubbles and strong shock waves that eventually lead to surface erosion [3]. A huge effort has been underway in various educational and research establishments over the last decade in trying to better predict the onset of cavitation in fuel injectors. The ultimate aim of the current research study is to achieve optimized designs of fuel injectors, where cavitation and flow boiling, together with their consequent erosion damage are minimized or even eliminated. In fuel injectors, cavitation and erosion damage have been known to occur mainly inside the injection nozzle holes and on the tip of the injector needle. Cavitation reduces the nozzle efficiency, affects the diesel spray pattern inside the engine cylinder and causes surface erosion phenomena which reduce the durability and performance of fuel injectors [1], [2].

Due to the difficulties of obtaining real time measurements of flow patterns inside the fuel injectors, significant effort has been put into the development of more accurate Computational Fluid Dynamics (CFD) cavitation models by various academic and industrial research teams around the world.

In this study, the latest non-isothermal version of the leading academic code GFS (Version 11) developed by the City University in London has been used to predict the onset of cavitation on three early development designs (Designs 1, 2 and 3) of a typical fuel injector.

In order to improve the accuracy of the predictions, the non-isothermal numerical model of diesel flow through the fuel injectors in GFS, now includes the effects of the variations of the properties of the diesel liquid as functions of both pressure and temperature as described by Kolev [4]. Furthermore by choosing the option of including the effect of viscous heating (generated by the viscous friction phenomena) within the enthalpy equation, the non-isothermal simulation results presented here are correctly taking into account the local temperature changes associated with the viscous heating and Joule-Thomson throttling effect [5] within the flow field.

In order to predict the fluid flow distributions of all variables under realistic transient conditions during one full injection cycle (encompassing the associated needle movement) and, more importantly, in order to avoid convergence difficulties during the transient CFD simulations, two preliminary sets of results are first obtained under steady state conditions:

1) The overall simulation strategy starts with the liquid phase (only) isothermal and hence constant property diesel flow under steady state conditions at the minimum axial needle lift position of 5µm (i.e. 5µm above the fully closed needle position).

2) The results from isothermal simulations are then used as initial conditions for the liquid phase (only) non-isothermal flow with variable properties as functions of both temperature and pressure, thus incorporating the correct enthalpy variation of the liquid phase as well as the viscous heating phenomena but once again under steady state conditions and at the same minimum axial needle lift position of 5µm.

3) The results from the non-isothermal steady state simulations are then used as initial conditions for the third and final stage of the calculations representing the fully transient cavitating diesel flow simulations spanning one full injection cycle. This cycle encompasses the actual needle movement and the associated computational grid change.

The simulation results presented here concentrate on those obtained during the second and third stages of the analyses.

A full description of the relationships between the saturation pressure and temperature of diesel liquid and the full set of equations outlining the variations of its variables properties as functions of both pressure and temperature as provided by Kolev [4], are given in Appendix A.

Definition of Geometry

Fig. 1 shows the 180 degree model geometry of Design 1 with its plane of symmetry passing through the centre of the fuel injector and Fig. 2 provides a zoomed-in view of the same half model geometry comprising of two and a half nozzles and showing the maximum axial lift position of the fuel injector needle with respect to its opposite needle seat surface. The full fuel injector geometry has 5 orifices, each set at a 72 degrees angle relative to each other.

Although some steady state CFD simulations of the diesel flow for this injector were originally started with this half model geometry, it soon became apparent that much faster turnaround time with almost no loss of accuracy could be achieved on a 72 degree section of the same fuel injector (encompassing just one nozzle orifice). Furthermore, by referring to Fig. 1, the high fuel pressure at the two actual inlet entries into the fuel injector geometry remains almost unchanged well past the spring mechanism.
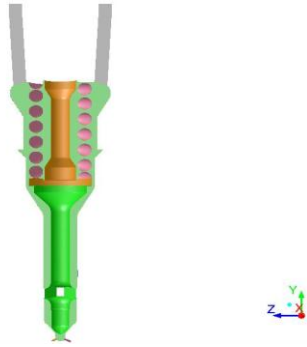
Figure 1. The half model geometry of Design 1, showing the two inlet flow paths, the spring mechanism and the needle.
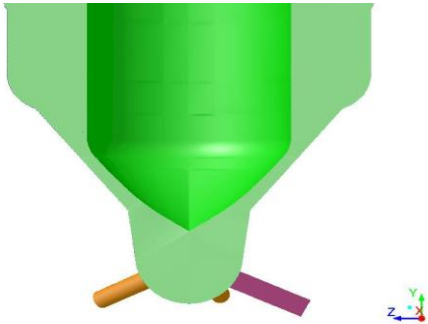

Figure 2. A zoomed-in view of the half model geometry of Design 1 showing the fuel injector needle at its maximum axial lift position.
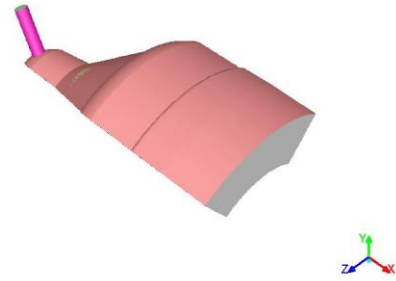

Figure 3. The 72 degree section of the Design 1 geometry, showing the pressure-inlet boundary and the pressure-outlet boundary downstream of the injector nozzle.
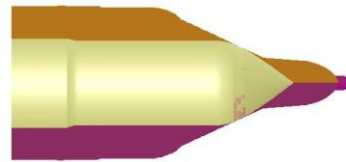

Figure 4. A second view of the 72 degree section of the Design-1 geometry showing the fuel injector needle at its minimum lift position and the two symmetry planes on either side of it.

Consequently, all CFD simulation results presented here correspond to this 72 degree section of the fuel injector geometry which has also been limited to a short axial distance upstream of the narrowest gap between the needle and its seat.

Fig. 3 shows the 72 degree section of the Design-1 geometry, while Fig. 4 provides a second view of the same geometry showing the fuel injector needle at its minimum axial lift position of 5µm above its fully closed position.

The non-isothermal CFD simulations of the diesel flow carried out in this study are based on the 72 degree sections of three different designs of the same fuel injector while it was going through its early stages of design and development phase. Figure 5 below present a zoomed-in view of the geometry profile on a cut plane through the centre of the fuel injector nozzle (at 5µm axial needle lift) for each of these three different designs 1 to 3.

1) The **Design 1** geometry has sharp edge entries into the injector nozzle (Fig. 5 blue)
2) The **Design 2** geometry has some minor differences in sac volume, needle profiles and nozzle outlet diameter with respect to Design 1, but more importantly has smooth entries into the injector nozzle (Fig. 5 red)
3) The **Design 3** geometry also has smooth entries into the injector nozzle (Fig. 5 green). However, the major difference between Design 3 and Designs 1 and 2 is the shape and size of the "sac volume" just upstream of the flow entry into the nozzle orifice. Fig. 5 clearly shows that the sac volume is in fact substantially smaller in Design 3 in comparison with Designs 1 and 2.
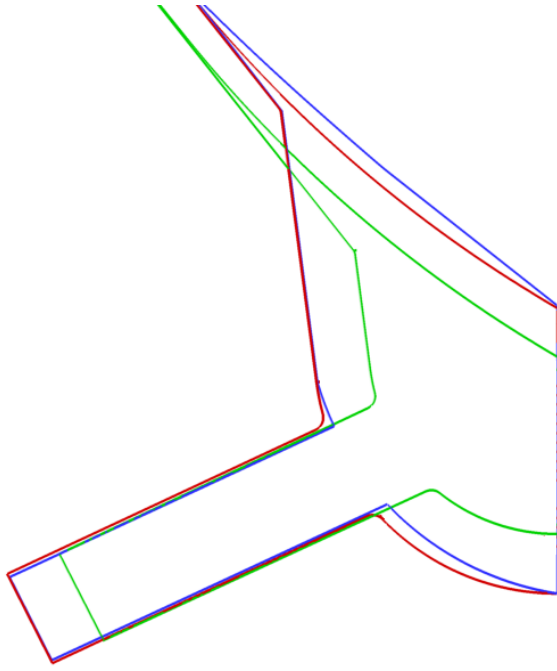
Figure 5. A zoomed-in view of the geometry profile on a cut plane through the centre of the fuel injector nozzle for all three designs; Design 1 is blue, Design 2 is red and Design 3 is green.

Numerical Modeling Approach

The cavitation model in GFS is based on an Eulerian Lagrangian approach. The numerical model uses the typical flow conservation equations in the Eulerian frame of reference for the continuous phase (liquid) while taking into account the effect of the dispersed phase volume fraction and employing a momentum exchange source term between the liquid and vapour phase [6]. For the dispersed (vapour) phase, cavitation is initiated through artificially created nuclei assumed to exist within the bulk of the flow, which subsequently grow into bubbles. The size of the initial nuclei is sampled from a probability density function. Once the pressure of the liquid phase falls below its saturation vapour pressure, the volume under tension is identified and the most probable locations for bubble nuclei formation are calculated randomly from a distribution function. The nuclei growing into bubbles undergo various physical processes which are taken into account by integrating the full Rayleigh Plesset equation and utilizing a stochastic Monte-Carlo approximation. In this cavitation model, the bubble coalescence and bubble to bubble interaction with momentum exchange during both bubble growth and collapse are all taken into account [6].

For the non-isothermal simulations, the most general form of enthalpy equation which includes the viscous heat dissipation term is solved iteratively where the values of ρ, k, C_p, v and h at every computational cell are updated from the equations given in Appendix A

using the latest calculated values of local p and T at any given iteration [7].

Flow and Thermal Boundary Conditions

In order to carry out a transient CFD analysis of diesel fuel flow within any fuel injector one needs to define the "axial needle lift profile" indicating how the axial needle lift changes with time during an injection cycle. This needle profile is then used to set up an appropriate dynamic mesh reflecting the actual location of the needle and thus the geometry of the flow domain at a given instance in time. The axial needle lift profiles for Design 1, 2 and 3 are shown in Fig. 6 below.
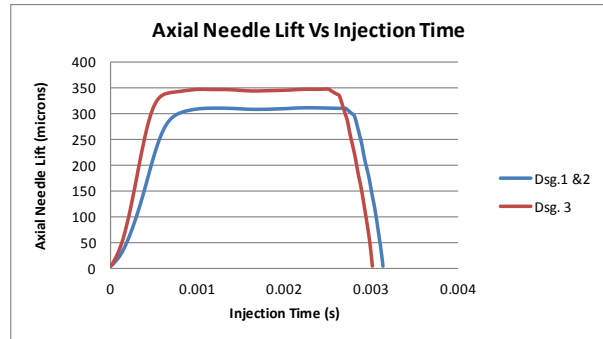

Figure 6. Axial needle lift profile for Designs 1, 2 and 3 during one injection cycle.

Fig. 6 clearly shows some differences in axial needle lift profiles for Design 3 in comparison with the other two designs. Designs 1 and 2 have a maximum lift of about 311.3µm and injection span time of about 3.14ms between a starting and ending axial needle lifts of 5µm. However, Design 3 has a maximum lift of about 346.8µm and injection span time of about 3.01ms between the same starting and ending axial needle lifts.

The experimental variations of the fuel rail pressure (i.e. the fuel injector inlet pressure) for Designs 1, 2 and 3 during the above injection span times are shown in Fig. 7 which confirms that there are indeed significant inlet fuel pressure variations during one injection cycle. For Designs 1 and 2, the maximum and minimum inlet fuel pressures are 162.91 and 189.75MPa respectively. Similarly, the maximum and minimum inlet fuel pressures for Design 3 are 160.70 and 189.84MPa respectively.

In order to provide the initial conditions for the transient cavitating diesel flow simulations the non-isothermal single phase steady state simulations were carried out at the minimum axial needle lift of 5µm, with a typical fuel inlet temperature of 80°C, a typical outlet (cylinder) pressure of 10MPa and an inlet fuel pressure corresponding to the minimum lift of 5µm extracted from the above inlet pressure profiles as shown in Table 1.

	Flow Boundary Conditions	Thermal Boundary Conditions
Pressure-inlet	Absolute pressure = 178.27MPa (Designs 1 & 2) Absolute pressure = 178.01MPa (Design 3) Turbulent velocity = 0.05m/s $\varepsilon = 0.2\text{E-03m}^2/\text{s}^3$	Static temperature = 353.15K = 80°C
Pressure-outlet	Absolute (cylinder) pressure = 10MPa	No reverse airflow was detected at this boundary. The temperature set at this boundary was therefore obsolete
Symmetry	Symmetry	Symmetry
Walls	No slip walls	Adiabatic external walls

Table 1. A full list of the steady state boundary conditions used for Designs 1, 2 and 3.
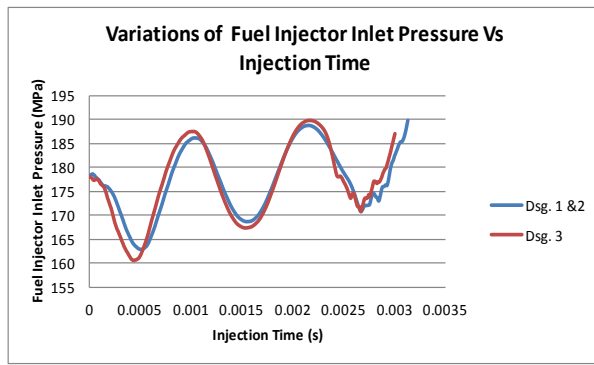

Figure 7. Inlet pressure profile for Designs 1, 2 and 3 during one injection cycle.

For the transient cavitating flow simulations, the pressure inlet boundary condition was made to vary according to Fig. 7. All other boundary conditions remained the same as those for steady state simulations and thus remained unchanged with respect to time (as shown in Table 1).

During these simulations, cavitation or change of phase from diesel liquid to diesel vapour was assumed to occur when the diesel liquid pressure fell below a constant saturation pressure of 610Pa. GFS code developers, suggested that a variable saturation pressure as a function of temperature may hinder stability and convergence with very little improvement on the accuracy of the cavitation predictions. Therefore in order to improve the stability of the analysis, the relationship between the saturation pressure and temperature given by equation (A.1) in Appendix A was not incorporated into the transient cavitation CFD simulations here. Instead, in order to bring about the onset of cavitation within the flow field a constant saturation pressure of 610Pa was used.

Grid/Mesh Structure

The computational mesh for Design 1 with sharp edge entries into the injector nozzle was fully hexahe-dral and at minimum axial needle lift consisted of 534,436 cells with six (6) mesh layers in the minimum gap between the needle and its opposite wall (giving a minimum cell size of 0.83µm). On the other hand, the computational mesh for Designs 2 and 3 with smooth entries into the injector nozzle was a hybrid consisting of tetrahedral computational cells within the inner sac volume and hexahedral ones elsewhere. The total number of computational cells for Designs 2 and 3 at minimum axial needle lift were 594,043 and 539,174 respectively but this time with ten (10) hexahedral mesh layers in the minimum gap region (for a minimum cell size of 0.5µm).

For the transient CFD simulation a dynamic mesh strategy was developed. For each fuel injector design, a set of five different mesh at five different axial needle lifts ranging from near minimum to near maximum lift positions were created. Each mesh is stretched within a specified range of axial needle lifts, before it being replaced with the next mesh corresponding to the next range of axial needle lifts, while at the same time the CFD solution data is interpolated from the current mesh to the next.

Since GFS is not parallelized, computations were limited to the use of a single CPU (on a Windows 7 platform) and hence rather long solution times. For the initial isothermal and the following non-isothermal steady state runs, the solution times were less than one (1) and four (4) days respectively. However for the transient simulations, the computational run time was substantially longer i.e. between 3 to 4 weeks.

Solution Method

As explained above, Kolev's equations of variable material properties for diesel liquid and the implementation of the enthalpy equation are already available within GFS and can be turned on by appropriately modifying the input file of the GFS solver. The turbulence model was based on their default standard k-ε model

with standard wall functions. The solution method was based on their "PISO" pressure correction scheme.

For the steady state simulations it was possible to use more accurate discretization schemes ("JASAK" discretization scheme for the momentum equation and "HYBRID" discretization scheme for each of the turbulent kinetic energy k, the turbulent dissipation rate ε and the energy equation).

However for the transient simulations only the "FOU" (First Order Upwind) discretization scheme was possible for the momentum, turbulent kinetic energy k, and turbulent dissipation rate ε equations while still being able to use the more accurate "HYBRID" convergence scheme for the energy equation. The switch from more accurate discretization schemes to the first order upwind scheme for momentum and turbulence equations became necessary due to convergence difficulties with the higher order schemes.

The time step for transient simulations started from 2.5μs at the start of the analyses and during the needle opening period. The time step was then increased to 8.0μs during the period when the needle was near its maximum axial lift. For the needle closing period, it became necessary for the time step to be decreased first to 6.0 then to 2.0 and finally to 1.0μs in order to achieve converged solutions. The number of inner iterations (per time step) was set to 100 at all time steps except for the final stages of the transient run, when the time step had been reduced to 1.0μs. For these time steps, the number of inner iterations was set to 200, in order to achieve convergence.

Steady State Non-Isothermal Single Phase Flow Results

Figs. 8 to 10 present zoomed-in views of the pressure, velocity and temperature distributions for the steady state non-isothermal simulations (at minimum axial needle lift of 5μm) on a cut plane through the centre of the fuel injector nozzle for Design 2 as obtained with City University's GFS code. Similar contour and vector plots were obtained for Designs 1 and 3.

The colour contour plots in Figs. 8 and 10 clearly show how the fuel pressure and temperature change rapidly across the minimum gap between the needle and its seat from the upstream high pressure and low temperature region to the downstream low pressure and high temperature region.

Tables 2 and 3 summarize some of the key results of the steady state non-isothermal single phase flow through Designs 1, 2 and 3. Table 2 includes the minimum pressure, maximum velocity, minimum and maximum temperature for the flow field together with the

mass weighted average outlet temperature and hence the temperature rise ΔT between the inlet and outlet boundaries. Table 3 shows a comparison of the predicted mass flow rate m through the nozzle orifice and the associated coefficient of discharge C_d calculated from the following equation:

$$C_d = \frac{\dot{m}}{A_{out}\sqrt{2\rho_{out}\Delta p}} \qquad (1)$$

Where A_{out} is the nozzle orifice outlet cross sectional area, D_{out} is the nozzle orifice outlet diameter, ρ_{out} is the diesel fuel density at the outlet boundary and Δp is taken as the pressure difference between the inlet and outlet boundaries.

These results indicate that at minimum axial needle lift of 5μm and based on the steady state single phase flow assumption, Design 1 shows the highest mass flow rate and hence the highest coefficient of discharge. However the minimum pressure value within the gap between the needle and the seat is negative only for Design 1, indicating that this design is the most susceptible one for the cavitation phenomena to occur in the minimum gap region.
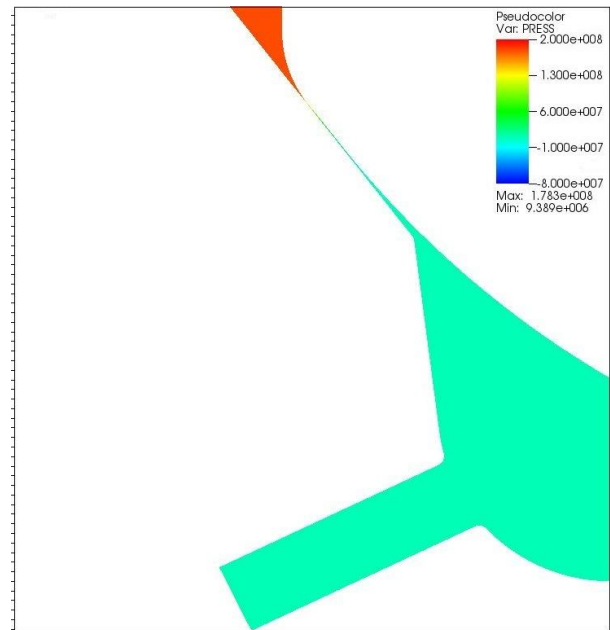

Figure 8. A zoomed-in view of the steady state pressure distribution on a cut plane through the centre of the fuel injector nozzle at minimum axial needle lift of 5μm; Design 2.

Injector Design	Minimum p (Pa)	Maximum V (m/s)	Maximum T (K)	Minimum T (K)	Average Outlet T (K)	ΔT (K)
Design 1	-6.38E+06	322.6	431.8	353.0	427.2	74.0
Design 2	9.39E+06	180.1	427.3	353.1	427.0	73.8
Design 3	9.55E+06	175.8	427.1	353.1	427.0	73.8

Table 2. A comparison of the first set of key CFD results – Steady State, non-isothermal single phase flow for Designs 1, 2 and 3

Injector Design	m (kg/s)	A_{out} (m^2)	D_{out} (µm)	ρ_{out} (kg/m^3)	Δp (Pa)	C_d
Design 1	9.97E-04	9.34E-08	344.89	719.5	1682.7E+05	0.0217
Design 2	9.11E-04	10.74E-08	369.83	719.6	1682.7E+05	0.0172
Design 3	8.78E-04	10.14E-08	359.42	719.7	1680.1E+05	0.0176

Table 3. A comparison of the second set of key CFD results – Steady State, non-isothermal single phase flow for Designs 1, 2 and 3
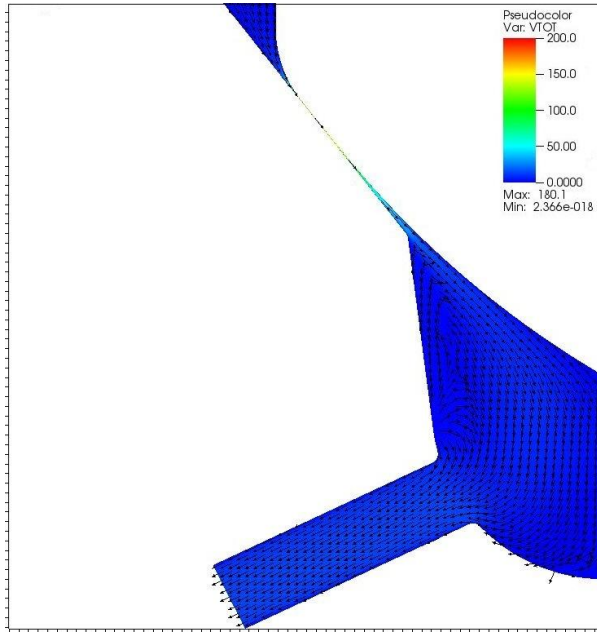

Figure 9. A zoomed-in view of the steady state velocity contours and vectors (uniformly located throughout the mesh and not scaled by magnitude) on a cut plane through the centre of the fuel injector nozzle at minimum axial needle lift of 5µm; Design 2.
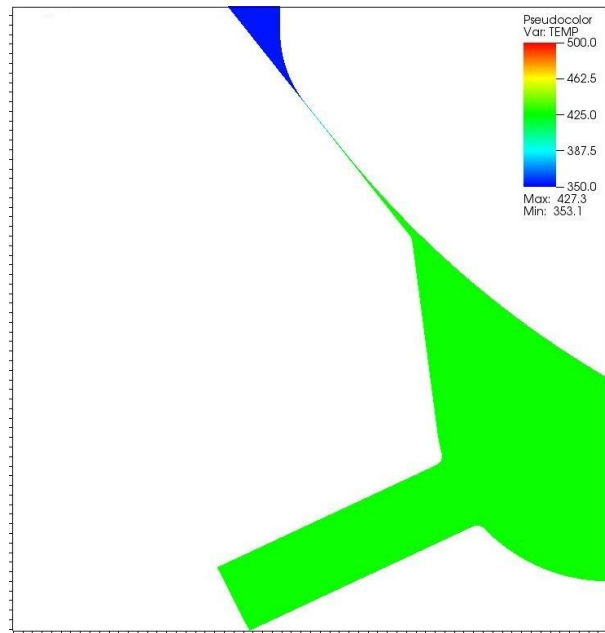

Figure 10. A zoomed-in view of the steady state temperature distribution on a cut plane through the centre of the fuel injector nozzle at minimum axial needle lift of 5µm; Design 2.

Transient Non-Isothermal Cavitating Flow Results

Figs. 11 and 12 present the variations of the diesel mass flow rate through the outlet cross section of the fuel injector nozzle and the variations of the coefficient of discharge during one injection cycle for Designs 1, 2 and 3.

Fig. 11 clearly indicates substantially lower mass flow rates at or around the maximum axial needle lift for Design 1 in comparison with Designs 2 and 3. Bearing in mind that despite of the fact that the maximum axial needle lift is substantially higher for Design 3, Fig. 11 also confirms that the highest mass flow rate at or around the corresponding maximum axial needle lift

is through Design 2. Furthermore it is worth noting that the oscillations observed on the mass flow rate values at and around the maximum axial needle lift are mainly due the variations of the inlet fuel pressure.

Fig. 12 confirms that while the maximum value of the coefficient of discharge C_d corresponding to the maximum axial needle lift position is about 0.806 and 0.814 for Designs 2 and 3 respectively, the corresponding maximum value for the Design 1 is only about 0.716. This implies that the fuel delivery into the engine cylinder by Design 1 is not as efficient as the other two designs at and around the maximum axial needle lift.

Figs. 13 and 14 present the variations of the mass weighted average temperature through the outlet cross section of the fuel injector nozzle and the variations of the temperature rise ΔT across the fuel injector during one injection cycle for Designs 1, 2 and 3.
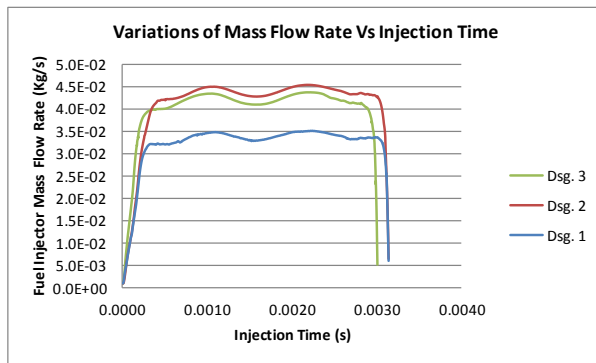

Figure 11. Mass flow rate variations through the outlet cross section of the fuel injector nozzle during one injection cycle; Designs 1, 2 and 3.
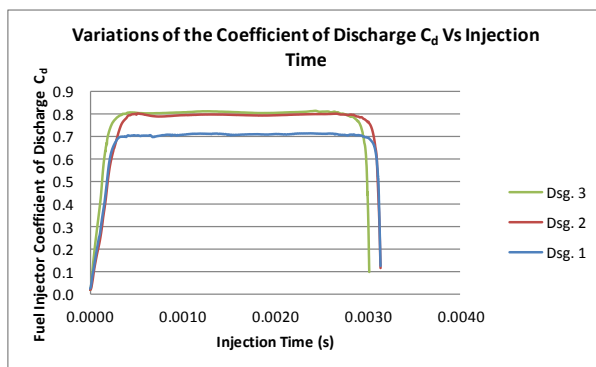

Figure 12. Variations of the coefficient of discharge for the fuel injector during one injection cycle; Designs 1, 2 and 3.
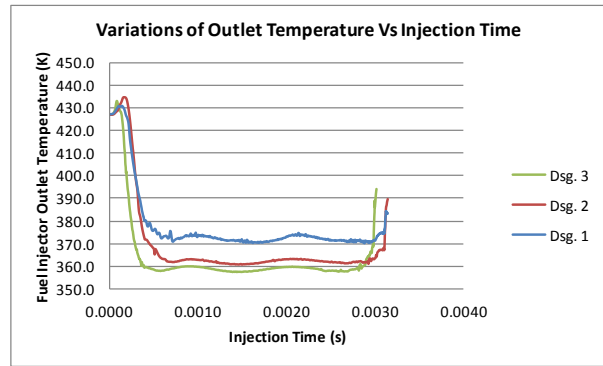

Figure 13. Variations of the mass weighted average nozzle outlet temperature during one injection cycle; Designs 1, 2 and 3.

Fig. 13 suggests that for a short duration after the start of the transient analysis, there is a further limited rise followed by a sharp decrease in the outlet temperature, as the axial needle lift increases towards its maximum value. The outlet temperature then remains almost constant depending on the value of the fuel inlet pressure (to within a few degrees) while the axial needle position is at or close to its maximum lift. However during the closing stages of the needle motion and as the axial needle lift decreases sharply with time, there is a sharp rise in the outlet temperature due to viscous heating effects. But it is worth noting that at a given axial needle lift position, the viscous heating effects reflected by the temperature rise across the fuel injector is less during the final needle closing stages in comparison with that during the early needle opening stages at the start of the transient analysis where the results of the steady state single phase flow were used as initial conditions. This discrepancy in temperature rise across the fuel injector suggests that the temperature distributions used as the initial conditions for the transient analysis based on the assumption of the needle remaining at its minimum axial lift under steady state conditions is unrealistic due to unrealistically high viscous heating effects predicted during the steady state analysis. This can also be confirmed by comparing the steady state temperature distributions within the sac volume and the fuel injector nozzle at the minimum axial needle lift of 5 μm (Fig. 10) with the corresponding temperature contour plots from the final time step of the transient simulations corresponding to the same axial needle lift (Fig. 25 below). As a result it is thought that the values of the temperature rise across the fuel injector obtained during the early needle opening stages are still affected by the initial conditions and should not be taken into considerations. Obviously as time increases, the effects of these unrealistic initial conditions are reduced [8]. For this reason and since additionally the steady state results also suffer from the unrealistic single phase flow assumptions, it is thought that the temperature and volume fraction results obtained during the closing needle

stages (i.e. from the maximum down to the minimum 5 μm needle lift positions) are more accurate for future comparison with experimental data.

Furthermore Fig. 13 also confirms that Design 3 shows the lowest nozzle outlet temperature at or around the maximum axial needle lift position and the greatest rise in the outlet temperature during the closing stages of the needle motion. Design 1 however has the highest nozzle outlet temperature at or around the maximum axial needle lift position but in comparison with the other two designs the rise in its outlet temperature during the closing stages is less pronounced and most importantly there is some minor cooling phenomena observed just before the axial needle lift is reduced down to the minimum 5μm position.
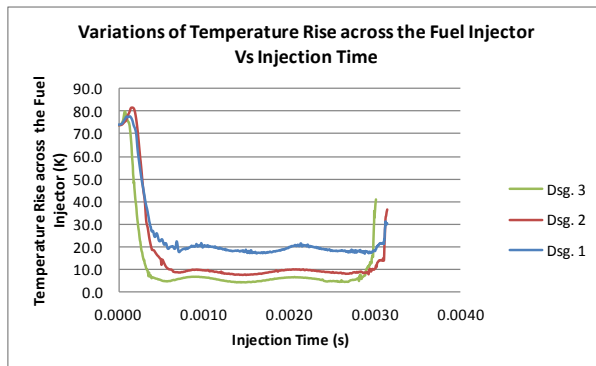

Figure 14. Variations of the temperature rise across the fuel injector during one injection cycle; Designs 1, 2 and 3.

Fig. 14 shows that the temperature rise across the fuel injector, as the needle closes and the axial needle lift is reduced to 5μm, is about 30.4, 36.5 and 40.9°C for Designs 1, 2 and 3 respectively. Furthermore the minimum temperature rise across the fuel injector corresponding to the maximum needle lift position is about 17.2, 7.6 and 4.1°C for Designs 1, 2 and 3 respectively.

Interestingly by referring to Figs. 11 to 12 and equation (1) and by considering the overall results at around the maximum axial needle position, the smaller nozzle outlet diameter in Design 3 has in fact brought about a slight increase in its coefficient of discharge in comparison with that of Design 2. This is despite of the fact that Design 3 is showing lower mass flow rate and at times higher diesel liquid density (at the outlet cross section) and higher pressure drop (across the fuel injector) at around the maximum needle lift position.

Furthermore by using numerical integration (trapezium rule) the areas under the curves shown in Fig. 11 provided the total mass of fuel delivered in one injection cycle which were 0.100, 0.129 and 0.120 g for Designs 1, 2 and 3 respectively. This confirmed that among the three designs considered here, Design 2 provides the largest fuel delivery in one injection cycle.

Figs. 15 to 17 show the temperature contour plots and Figs. 20 to 22 show the vapour volume fraction distributions at round the maximum axial needle lift for Designs 1, 2 and 3 respectively.
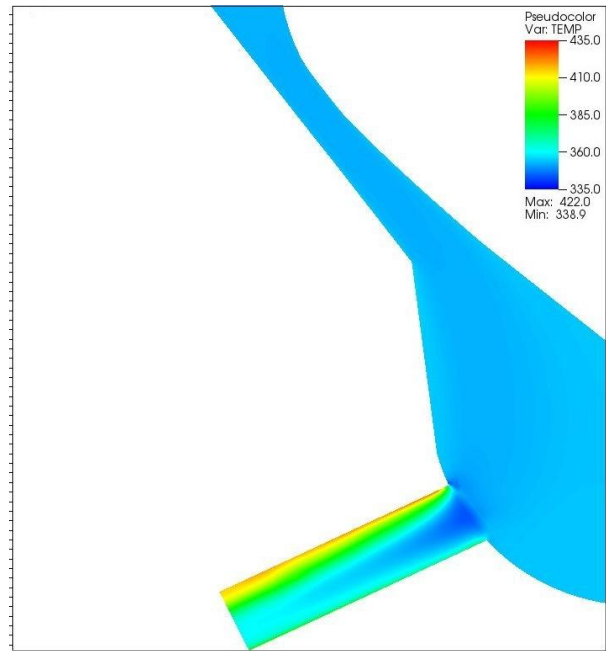

Figure 15. A zoomed-in view of the temperature distribution on a cut plane through the centre of the fuel injector nozzle at around the maximum axial needle lift of 310.5μm (closing stage); Design 1.
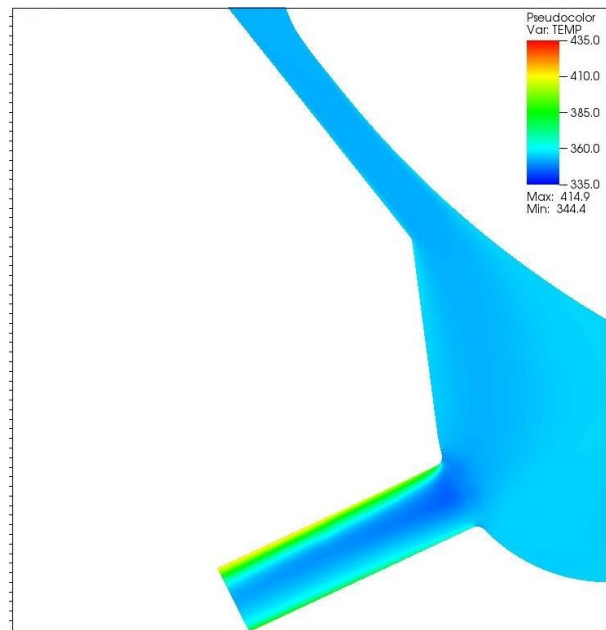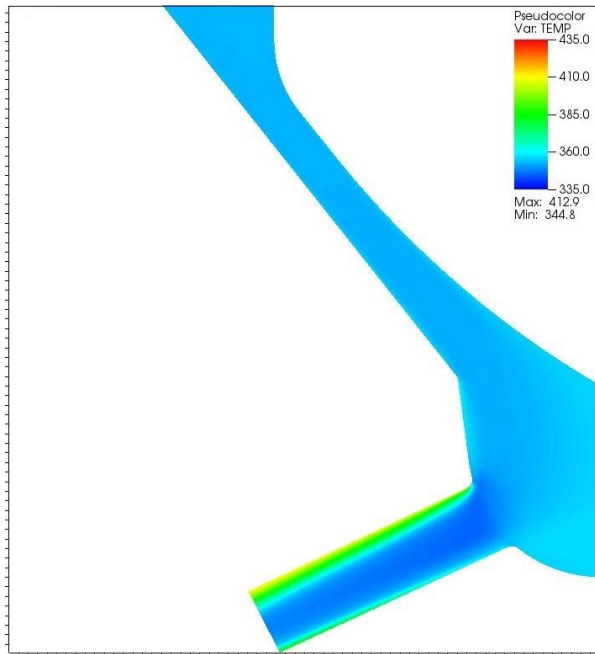

Figure 16. A zoomed-in view of the temperature distribution on a cut plane through the centre of the fuel injector nozzle at around the maximum axial needle lift of 310.5μm (closing stage); Design 2.

Figure 17. A zoomed-in view of the temperature distribution on a cut plane through the centre of the fuel injector nozzle at around the maximum axial needle lift of 346.4µm (closing stage); Design 3.
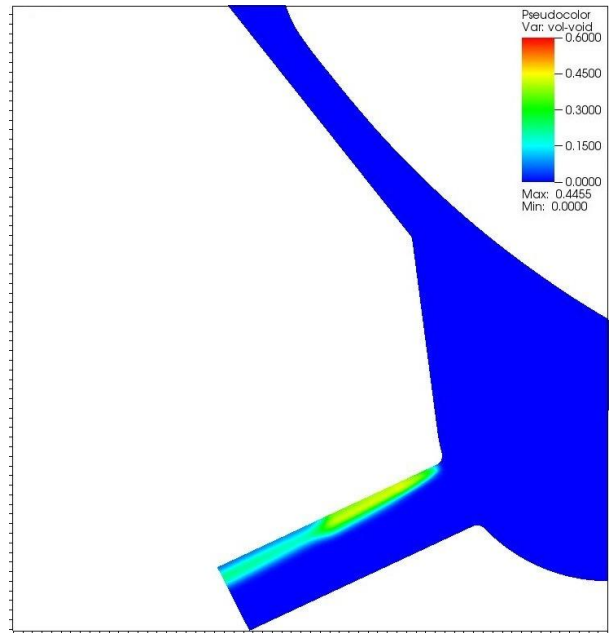

Figure 19. A zoomed-in view of the vapour volume fraction distribution on a cut plane through the centre of the fuel injector nozzle at around the maximum axial needle lift of 310.5µm (closing stage); Design 2.
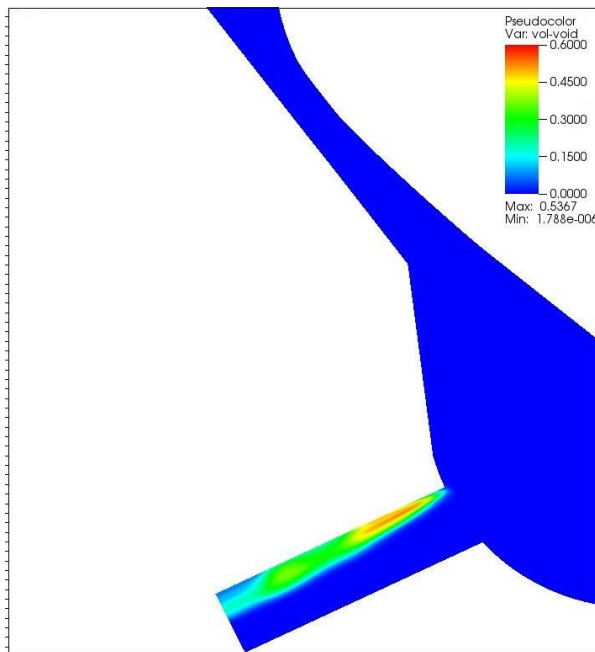

Figure 18. A zoomed-in view of the vapour volume fraction distribution on a cut plane through the centre of the fuel injector nozzle at around the maximum axial needle lift of 310.5µm (closing stage); Design 1.
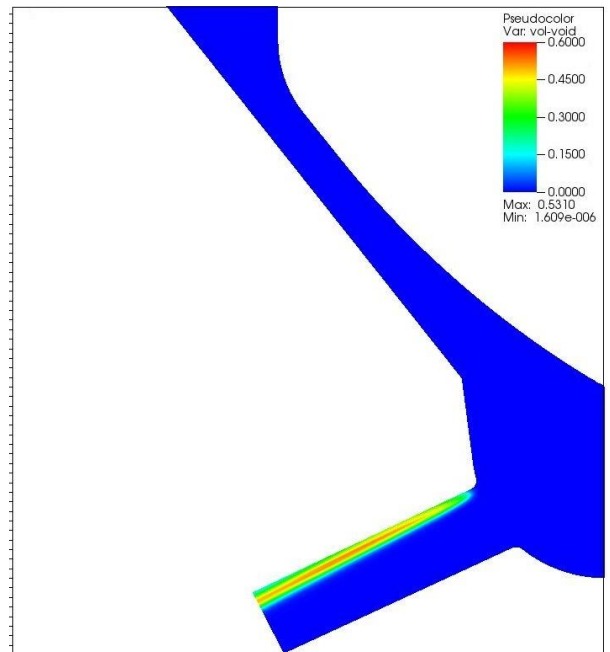

Figure 20. A zoomed-in view of the vapour volume fraction distribution on a cut plane through the centre of the fuel injector nozzle at around the maximum axial needle lift of 346.4µm (closing stage); Design 3.

The higher diesel temperature values observed in Figs. 15 to 17 close to the nozzle wall surfaces highlight the effects of viscous heating as diesel flows through such a narrow passage with very high velocities. Furthermore the distribution of the vapor volume fraction observed in Figs. 18 to 20 show how cavitation is formed at the fuel injector nozzle entry as very high diesel fuel pressure suddenly drops below its saturation vapour pressure value.

Figs. 21 to 23 show the amount of superheat ΔT_{Boil} and thus the potential regions of heterogeneous boiling at round the maximum axial needle lift for Designs 1, 2 and 3 respectively. They reveal that Design 3 has the smallest flow boiling region at the top entry into the fuel injector nozzle and the lowest maximum amount of superheat of just under 112°C. Here it is important to emphasize that in the absence of a flow boiling model during the actual CFD simulations, the results presented in Figs. 21 to 23 do not take into account of any interactions that might exist between cavitation and flow boiling within the same computational cell. Furthermore it is also important to realize that the amount of superheat could be significantly different under actual engine operating conditions where the adiabatic wall boundary conditions need to be replaced with more realistic values obtained from conjugate heat transfer analyses.
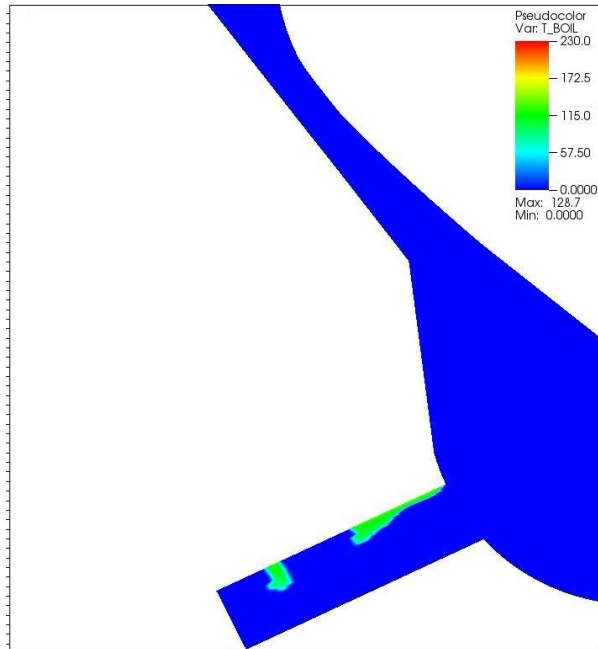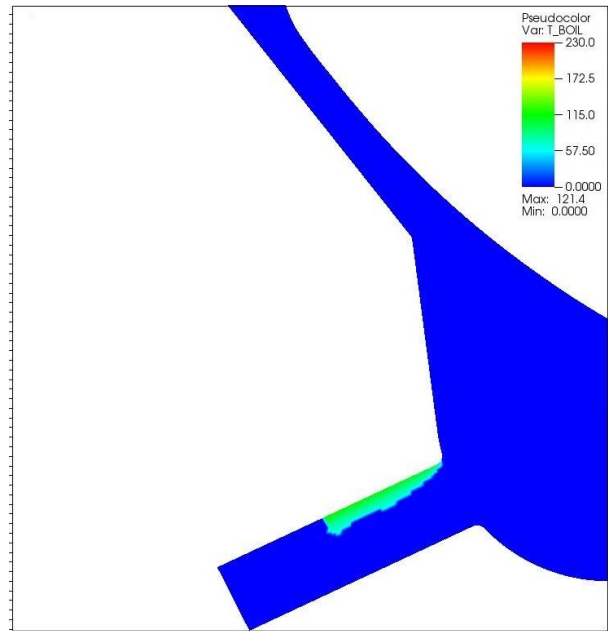

Figure 22. A zoomed-in view of the potential regions of flow boiling on a cut plane through the centre of the fuel injector nozzle at around the maximum axial needle lift of 310.5μm (closing stage); Design 2.
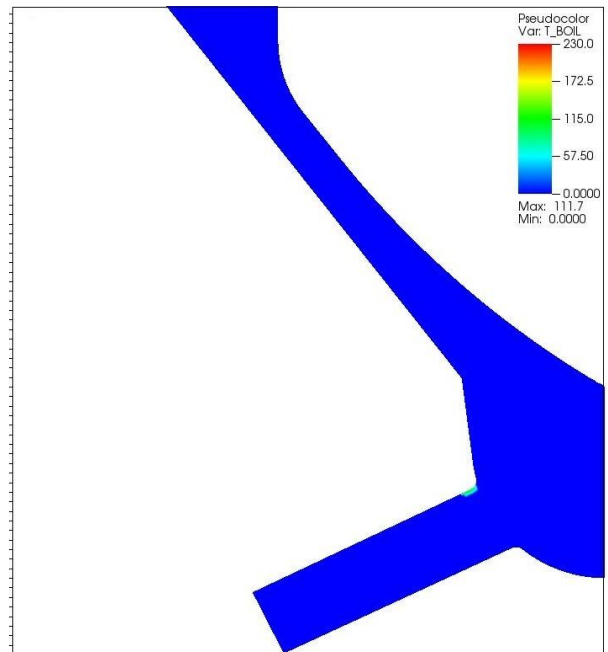

Figure 23. A zoomed-in view of the potential regions of mainly heterogeneous boiling on a cut plane through the centre of the fuel injector nozzle at around the maximum axial needle lift of 346.4μm (closing stage); Design 3.

Figs. 24 to 26 show the temperature contour plots and Figs. 27 to 29 show the vapour volume fraction distributions on a cut plane through the centre of the fuel injector nozzle at the closing minimum axial needle lift of 5μm for Designs 1, 2 and 3 respectively.

Figure 21. A zoomed-in view of the potential regions of flow boiling on a cut plane through the centre of the fuel injector nozzle at around the maximum axial needle lift of 310.5μm (closing stage); Design 1.

Figure 24. A zoomed-in view of the temperature distribution on a cut plane through the centre of the fuel injector nozzle at the minimum axial needle lift of 5µm (closing stage); Design 1.

Figure 26. A zoomed-in view of the temperature distribution on a cut plane through the centre of the fuel injector nozzle at the minimum axial needle lift of 5µm (closing stage); Design 3.
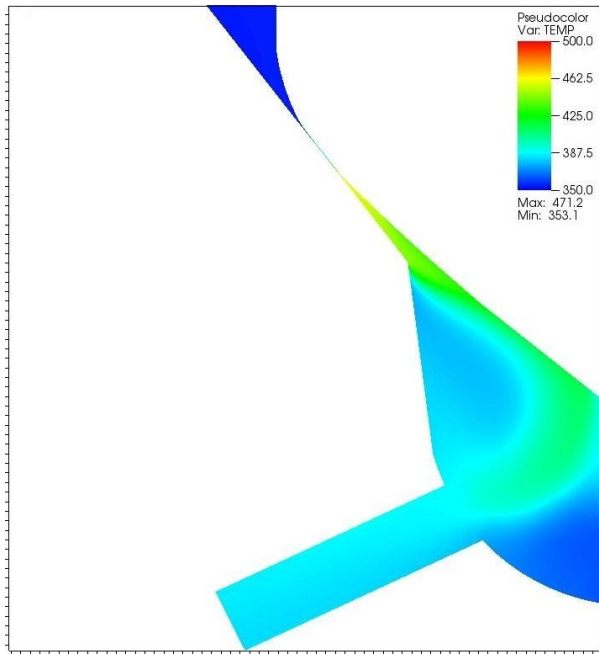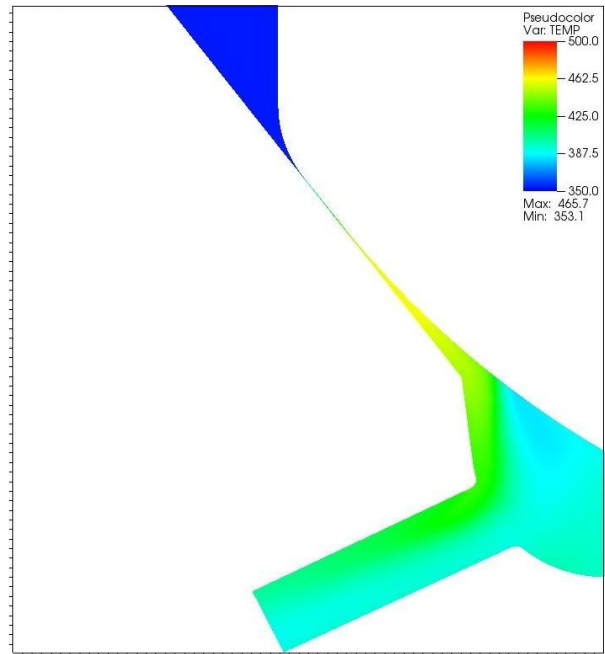

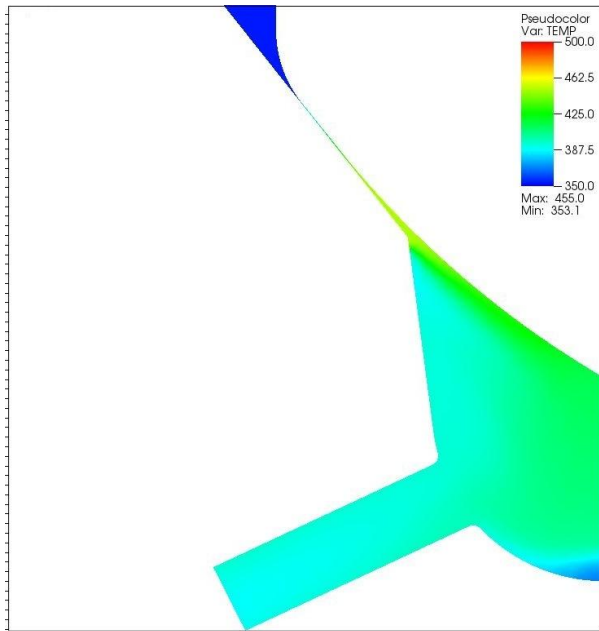**Figure 25.** A zoomed-in view of the temperature distribution on a cut plane through the centre of the fuel injector nozzle at the minimum axial needle lift of 5 µm (closing stage); Design 2.

Figure 27. A zoomed-in view of the vapour volume fraction distribution on a cut plane through the centre of the fuel injector nozzle at the minimum axial needle lift of 5µm (closing stage); Design 1.

Figure 28. A zoomed-in view of the vapour volume fraction distribution on a cut plane through the centre of the fuel injector nozzle at the minimum axial needle lift of 5µm (closing stage); Design 2.
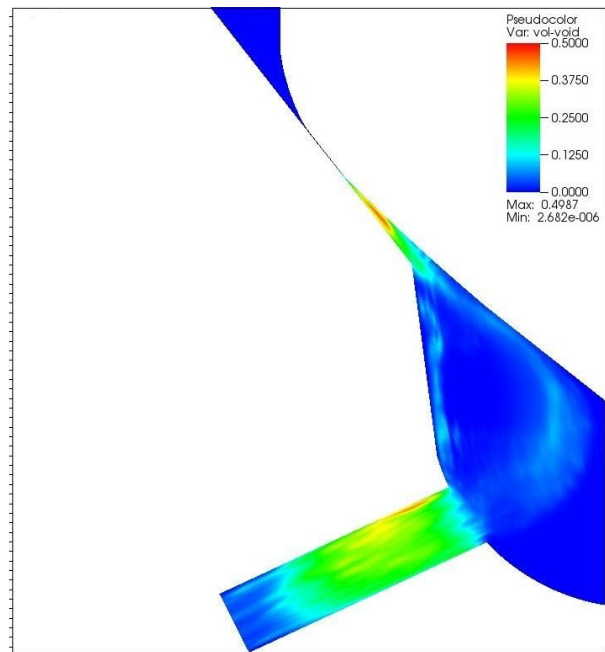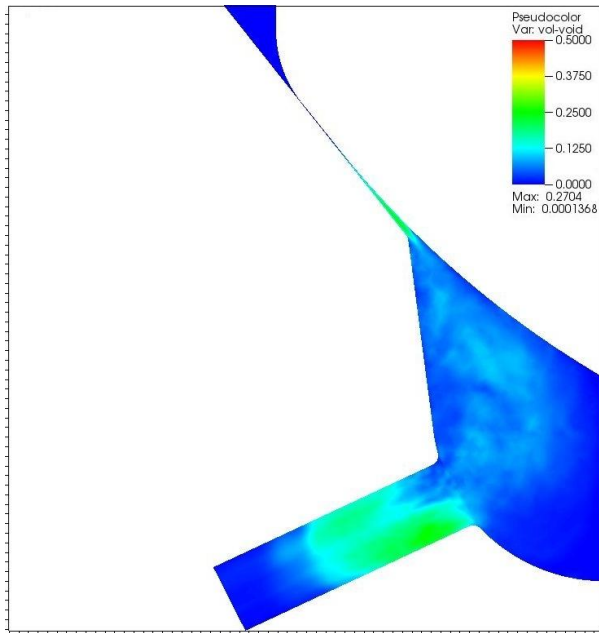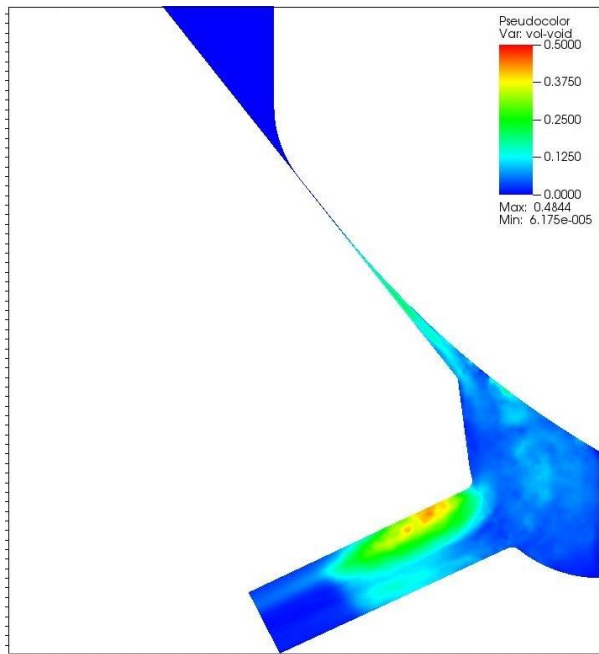

Figure 29. A zoomed-in view of the vapour volume fraction distribution on a cut plane through the centre of the fuel injector nozzle at the minimum axial needle lift of 5µm (closing stage); Design 3.

The higher diesel temperature values observed in Figures 24 to 26 within the minimum gap region between the needle and its seat once again highlight the effects of viscous heating as diesel flows through this narrow passage with very high velocities. This has sub-

sequently resulted in higher temperature values (in comparison with the inlet fuel temperature) both within the sac volume and the nozzle too. Furthermore the distribution of the vapor volume fraction observed in Figs. 27 to 29 show how cavitation is formed both within the minimum gap region and at the fuel injector nozzle entry as diesel fuel pressure drops below its saturation vapour pressure value.

Finally Figs. 30 to 32 show the corresponding amount of superheat ΔT_{Boil} and thus the potential regions of mainly heterogeneous boiling on a cut plane through the centre of the fuel injector nozzle at the closing minimum axial needle lift of 5µm for Designs 1, 2 and 3 respectively.

Figure 30. A zoomed-in view of the potential regions of flow boiling on a cut plane through the centre of the fuel injector nozzle at the minimum axial needle lift of 5µm (closing stage); Design 1.

The results in Figs. 30 to 32 reveal that apart from the minimum gap region between the needle and its seat where flow boiling is potentially predicted for all three designs, Design 2 shows the largest region of flow boiling but the lowest amount of maximum superheat at the bottom entry into the fuel injector nozzle. Interestingly Design 1 shows an isolated region of potential flow boiling in the middle of the sac volume.
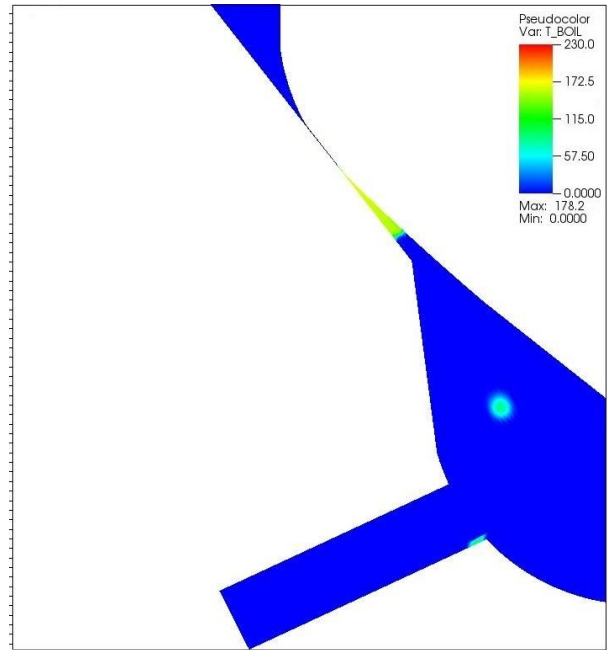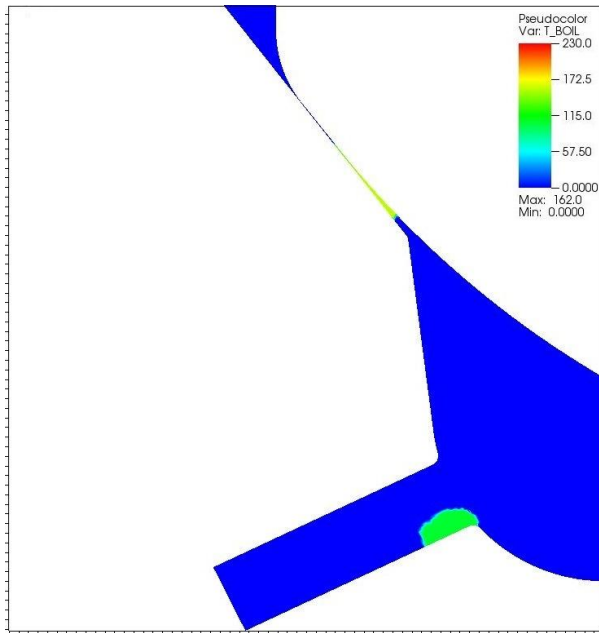
Figure 31. A zoomed-in view of the potential regions of flow boiling on a cut plane through the centre of the fuel injector nozzle at the minimum axial needle lift of 5μm (closing stage); Design 2.
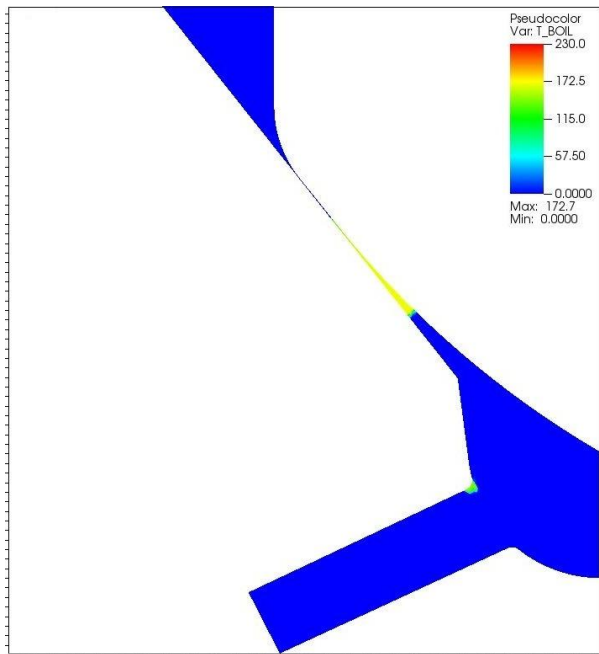

Figure 32. A zoomed-in view of the potential regions of mainly heterogeneous boiling on a cut plane through the centre of the fuel injector nozzle l at the minimum axial needle lift of 5μm (closing stage); Design 3.

Conclusions

The results of a non-isothermal and cavitating (two phase) transient simulation of diesel flow within each of the three development phase designs of a fuel injector has been obtained during one injection cycle starting

from the minimum axial needle lift position of 5μm, up to the maximum lift position and back down to the same minimum lift location. The simulations have been carried out using the leading academic CFD code for cavitation (City University's GFS). The transient simulations were based on the use of variable properties for diesel liquid (as functions of both pressure and temperature) as provided by Kolev [4]. Additionally, the effects of viscous heating were also included in order to further improve the accuracy of the physics of the flow field within such fuel injectors.

The main objective of this part of the overall research study presented here, was to better understand the effects of viscous heating and variable properties, on the extent of the diesel vapour formation (and its subsequent distribution) as a result of cavitation within the three fuel injector designs considered here and to have an initial evaluation of the likelihood of the occurrence of heterogeneous and homogenous flow boiling within the flow field.

The initial conditions used for the transient cavitating diesel flow simulations were based on the results of the non-isothermal single phase steady state simulations carried out at the minimum axial needle lift of 5μm, with a typical fuel inlet temperature of 80°C, a typical outlet pressure boundary condition of 10MPa and an inlet pressure boundary condition corresponding to the minimum lift of 5μm extracted from the inlet pressure profiles Fig. 7.

The overall mass flow rate results of the transient simulations (Fig. 11) clearly indicate that in comparison with Designs 2 and 3, there is substantially lower mass flow rate at or around maximum axial needle lift for Design 1, while at around the same maximum axial needle position they show 4.3% higher maximum mass flow rate through Design 2 (45.5g/s) in comparison with that through Design 3 (43.6g/s). This is thought to be mainly due to about 2.9% larger nozzle diameter in Design 2. Furthermore the amounts of total fuel mass delivered in one injection cycle were 0.100, 0.129 and 0.120g for Designs 1, 2 and 3 respectively.

In non-dimensional terms, the maximum Reynolds number (*Re*) values calculated at the outlet cross sectional area of the fuel injector nozzle at or around the maximum axial needle lift position were $1.36^{.}10^{5}$, $1.51^{.}10^{5}$ and $1.47^{.}10^{5}$ for Designs 1, 2 and 3 respectively.

Similarly by comparing the variations of the coefficient of discharge, shown in Fig. 12 one finds that the maximum value of this coefficient at around the maximum axial needle lift position is substantially lower for Design 1 (C_d=0.716) in comparison with the corresponding values for Design 2 (C_d=0.806) and Design 3 (C_d=0.815), thus implying that the fuel delivery into the engine cylinder is not as efficient for Design 1 as it is for the other two designs. The smaller nozzle outlet diameter for Design 3 has in fact brought about a slight

increase in its coefficient of discharge in comparison with that of Design 2, despite of the latter showing higher mass flow rate and at times lower diesel liquid density (at the outlet cross section) and lower pressure drop (across the fuel injector) at around the maximum needle lift position.

The variations of the nozzle orifice outlet temperature during the injection cycle (Fig. 13), for all three designs, show a limited rise for a short duration after the start of the transient analysis, followed by a sharp decrease, as the axial needle lift increases towards its maximum value. The outlet temperature then remains almost constant (to within a few degrees) while the axial needle position is at or around its maximum axial lift position. However during the closing stages of the needle motion and as the axial needle lift decreases sharply with time, there is a sharp rise in the outlet temperature due to viscous heating effects. But at a given axial needle lift position; the viscous heating effects observed during the closing stages of the needle motion reflected by the sac volume and nozzle orifice temperature is less than that observed at the start of the analysis where the results of an unrealistic steady state single phase flow analysis was used as initial conditions. For this reason it is thought that temperature and volume fraction results obtained during the opening needle stages (i.e. from the minimum 5µm up to the maximum needle lift positions) are not accurate enough for future comparisons with experimental data. Thus by focusing on the results of the transient analysis over the second half of the injection cycle, one can see that the temperature rise across the fuel injector as the needle closes and as the axial needle lift is reduced to 5µm, is about 30.4, 36.5 and $40.9^{o}C$ for Designs 1, 2 and 3 respectively. Furthermore the minimum temperature rise across the fuel injector corresponding to the maximum needle lift position is about 17.2, 7.6 and $4.1^{o}C$ for Designs 1, 2 and 3 respectively.

As a result of the inaccurate nature of the initial conditions, it is thought that ideally a further injection cycle should be simulated, this time based on the results of the final time step from the current transient simulations (i.e. at the 5µm minimum axial needle lift obtained at the end of the closing stage of the needle motion) and used as the initial conditions for the following second injection cycle. However in the simulation scenarios considered in this research study, the implementation of such approach may face some further difficulties because the measured inlet pressure boundary values at the start and the end of the injection cycles are quite different. But for the forthcoming planned transient simulations based on a constant inlet pressure boundary value of 300MPa, such difficulties do not exist and this approach could be implemented more easily.

The overall results of the transient cavitation simulations presented here, show that at low axial needle lifts and in all three designs, cavitation occur not only within the narrow gap between the needle and the seat but also on both the top and bottom surfaces of the nozzle orifice. However by comparing the amount of diesel vapour volume produced (as a result of cavitation) and its distribution within the flow field close to the the top and bottom surfaces of the fuel injector nozzle in Designs 2 and 3, the risk of erosion (as a result of diesel vapour bubble collapse) on the bottom nozzle surface is higher for Design 2 and lower for Design 3. Overall at low axial needle lifts, among the three designs considered here, Design 1 shows the highest erosion risk on the surfaces of the needle and the needle seat while Designs 1 and 3 show higher erosion risk on the top nozzle surface in comparison with Design 2.

On the other hand at high axial needle lifts diesel vapour formation and distribution occur mainly on the top surface of the fuel injector nozzle, and among the three designs, Design 2 is showing the lowest amount of vapour volume fraction in that region.

By isolating the relevant local pressure regions within the flow field corresponding to the known and applicable range of approximately 9 to 3000kPa for the saturation vapour pressure of diesel, and using the known relationship between the saturation temperature and saturation vapour pressure of diesel, the regions where the local temperature exceeds the saturation temperature were identified. The positive difference between the local temperature and saturation temperature in these regions identified the amount of superheat and hence the potential regions of heterogeneous boiling close to the fuel injector wall surfaces and homogeneous boiling in the bulk of liquid.

The maximum amount of superheat obtained at around the maximum axial needle lift was about 129, 121 and $112^{o}C$ for Designs 1, 2 and 3 respectively where all potential regions of heterogeneous boiling were on the top surface of the fuel injector nozzle. However at the minimum axial needle lift of 5µm, the amount of superheat was significantly higher at about 178, 162 and $173^{o}C$ for Designs 1, 2 and 3 respectively where the potential regions of heterogeneous boiling were both within the minimum gap between the needle and its seat and either at the bottom (Design 1 and 2) or top (Design 3) entry region into the fuel injector nozzle.

Here it is important to emphasize that since we are considering adiabatic wall boundary conditions, the heat flux to and from the walls (which would naturally affect the amount of superheat) have been neglected. For this reason further follow up analyses with constant wall temperature and conjugate heat transfer are planned to further enhance the qualitative hint provided in this paper about the presence of flow boiling in fuel injectors under actual engine operating conditions.

It is thought that in order to better predict the onset of erosion on the fuel injector walls, attention should be paid to the locations of not only the cavitation regions but also the potential heterogeneous boiling regions.

The collapsing locations of diesel vapour bubbles generated by both phenomena identified by a combination of negative volume fraction gradients and positive pressure gradients within the flow field [3] should provide a more accurate prediction of erosion locations. This will be the subject of the next stage of the current research study.

Overall, based on the current three sets of transient non-isothermal cavitating flow results carried out for the three development phase designs of the fuel injector used in this study, Design 2 shows the highest mass flow rate and the lowest amount of diesel vapour volume (produced as a result of cavitation) at its maximum axial needle lift of 310.5μm and the highest amount of fuel delivery into the engine cylinder over one injection cycle. However Design 3 shows the lowest viscous heating and the smallest region of possible heterogeneous boiling at its maximum axial needle lift of 346.4μm. Furthermore Design 3 shows slightly higher coefficient of discharge at its maximum axial needle lift in comparison with Design 2. At the minimum axial needle lift of 5μm, Design 2 shows the smallest region of high vapour volume fraction developed as a result of cavitation and the lowest viscous heating effects within the nozzle orifice while Design 3 is still showing the smallest region of possible heterogeneous boiling. In summary, while Designs 2 and 3 are generally superior to Design 1 in terms of higher and more efficient fuel delivery, more confined volumes of diesel vapour within the flow field and smaller flow boiling regions, between them there is no clear cut winner.

Therefore although the present results should be considered as preliminary and the transient simulation runs should ideally be extended for another injection cycle to minimize the impact of the steady state initial conditions, by capturing the locations of both cavitation and, for the first time, the heterogeneous flow boiling within the fuel injector tip and nozzle holes, the CFD is proving to be a valuable design tool in supporting the selection of the most appropriate fuel injector design. Although GFS predictions have been validated for a variety of different experimental set ups, an experimental validation for the very critical conditions examined in this paper has not yet been carried out.

The follow on work that has already been completed and will be published soon includes a further second set of transient simulation runs, where the constant 10MPa pressure outlet boundary will be replaced with a time variable one based on the measured cylinder pressure data available during the injection cycle, while at the same time replacing the adiabatic boundary walls with at least a more realistic constant injector boundary wall temperature of 180°C. These boundary wall temperatures will in turn be later replaced by those obtained from the results of the conjugate heat transfer simulations currently underway within this overall research project.

There is also a third set of transient simulation runs, where the time variable pressure inlet boundary will be replaced with a much higher but constant fuel pressure inlet boundary value of 300MPa in order to investigate the impact of higher fuel pressure on the temporal variations of the mass flow rates, temperature distributions, the amount of diesel vapour volume produced and distributed within the flow field (as a result of cavitation) and the locations of heterogeneous boiling regions. This work has also been completed and results will be published soon.

Nomenclature

Symbol	Physical meaning
A_{out}	Nozzle outlet cross sectional area (m^2)
C_p	Specific heat capacity (J/kg K) (at constant pressure)
C_d	Coefficient of discharge
D_{out}	Nozzle outlet diameter (μm)
k	Thermal conductivity (W/m K)
h	Specific enthalpy (J/kg)
M	Molecular weight (kg/mole)
p	Absolute pressure (Pa)
p_{ref}	Kolev's reference pressure (Pa)
p_{sat}	Saturation pressure (Pa)
R	Ideal gas constant (J/kg K)
Re	Reynolds number
s	Specific entropy (J/kg K)
T	Static temperature (K)
T_{ref}	Kolev's reference temperature (K)
T_{sat}	Saturation temperature (K)
ΔT	Temperature rise across the fuel injector (K)
ΔT_{Boil}	Temperature rise over saturation temperature (K)
ν	Kinematic viscosity (m^2/s)
η	Dynamic viscosity (Pa s)
ρ	Density (kg/m^3)

References
1)   Gavaises, M., *Flow in valve covered orifice nozzles with cylindrical and tapered holes and link to cavitation erosion and engine exhaust emissions*, International Journal of Engine Research, Vol. 9, p.435-447 (2008).
2)   Gavaises, M., Papoulias, D., Andriotis, A., Giannadakis, E., Theodorakakos, A., *Link between cavitation development and erosion damage in diesel*

injector nozzles, SAE Technical Paper 2007-01-0246, (2007).

3)   Bergeles, G., Koukouvinis, P.K., Gavasies, M., *A cavitation aggressiveness index (CAI) within the RANS methodology for cavitation flows*, Proceedings of the 11th International Conference on Hydrodynamics October 2014.

4)   Kolev, N.I., *Multiphase Flow Dynamics 3: Turbulence, Gas Absorption and Release, Diesel Fuel Properties:* Springer Verlag Berlin Heidelberg, 2002.

5)   Cengel, Y., Boles, M., *Thermodynamics: An Engineering Approach*, 5th Edition, McGraw-Hill, 2006, p.239 & 668.

6)   Giannadakis, E., Gavaises, M., Roth, H., Arcoumanis, C., *Cavitation modelling in single-hole diesel injector based on Euleian-Lagrangian approach*, Thiesel 2004 Conference on Thermo and Fluid Dynamic Processes in Diesel Engines, 2004.

7)   Theodorakakos, A., Strotos, G., Mitroglou, N., Atkin, C., Gavaises, M., *Friction-induced heating in nozzle hole micro-channels under extreme fuel pressurization*, Fuel 123, p.143-150, (2014).

8)   Strotos, G., Koukouvinis, P., Theodorakakos, A., Gavaises, M., Bergeles, G., *Transient heating effects in high pressure diesel injector nozzles*, International Journal of Heat and Fluid Flow, Volume 51, p. 257-267, (2015).

9)   Kandikar, S.G., Shoji, M., Dhir, V.K., *Handbook of Phase Change: Boiling and Condensation*, June 1999, p.79.

10)   Bankoff, S.G., Mikesell, R.D., *Growth of bubbles in a liquid of initially non uniform temperature*, ASME-58-A-105, (1958).

APPENDIX A

Diesel Fuel Saturation Pressure and Temperature

The variations of diesel liquid saturation vapour pressure and saturation temperature are provided by equation (A.1) below [4]. Based on this relationship at a given local temperature, cavitation would occur if the local pressure falls below the saturation vapour pressure given by the following equation:

$$p_{sat} = -1.1510 * 10^3 + 14.339 T_{sat} - 6.9960 * 10^{-2} T_{sat}^2 + 1.6928 * 10^{-4} T_{sat}^3 - 2.1708 * 10^{-7} T_{sat}^4 + 1.4186 * 10^{-10} T_{sat}^5$$
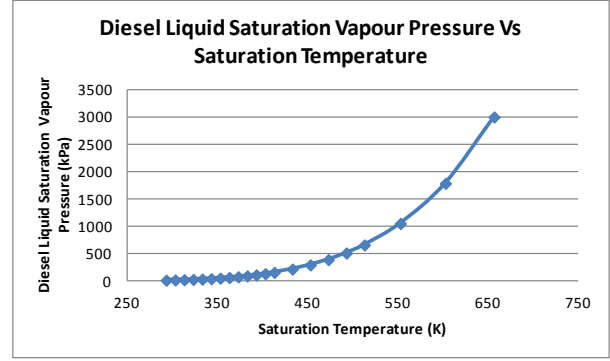
(A.1)

Figure A1. Variations of diesel liquid saturation pressure with saturation temperature.

Based on the same set of data, a corresponding equation (A.2) has been derived to provide the variations of the saturation temperature with saturation vapour pressure. According to this equation at a given local pressure, flow boiling could potentially occur if the local temperature rises above the saturation temperature given by equation (A.2) and the higher the temperature rises above the saturation temperature (i.e. the higher the amount of superheat) the higher is the chance of flow boiling to occur.

$$T_{sat} = \exp(6.352410 - 6.41213 * 10^{-1} \ln(p_{sat}) + 1.480561 * 10^{-1} (\ln(p_{sat}))^2 - 1.597815 * 10^{-2} (\ln(p_{sat}))^3 + 9.443721 * 10^{-4} (\ln(p_{sat}))^4 - 2.710023 * 10^{-5} (\ln(p_{sat}))^5 + 2.766986 * 10^{-7} (\ln(p_{sat}))^6)$$
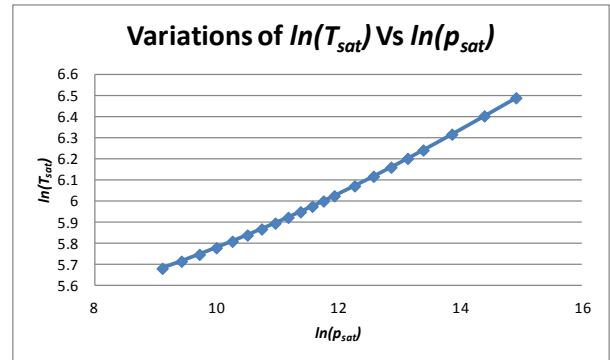
(A.2)

Figure A2. Variations of $ln(T_{sat})$ against $ln(p_{sat})$.

The nucleation process in flow boiling can in general be divided into two categories of homogeneous and heterogeneous boiling [9]. The homogeneous boiling refers to the formation of bubbles in superheated liquid in the absence of any pre existing gas or vapour nuclei and away from any solid surfaces. The heterogeneous boiling is the process in which bubbles form discretely on the pits, scratches and grooves on a heated surface submerged in a pool of liquid. According to the work of

Bankoff [10], the superheats associated with heterogeneous boiling are much smaller than those associated with the homogenous boiling.

In this study and in the absence of a fully developed flow boiling model for diesel liquid, by post processing the two phase flow transient CFD simulation results at a given time step, the local diesel pressure values at any given location within the CFD model which correspond to the range of the saturation pressure values (9.036 to 3000kPa) corresponding to Fig. A1 are isolated from the pressure domain field as shown below:

$$p_A = \max(p, 9036) \tag{A.3}$$

$$p_{sat} = \max(p_A, 3E06) \tag{A.4}$$

For these isolated pressure values, the corresponding saturation temperature values are calculated from equation (A.2) above. The positive difference between the local temperature and saturation temperature values at the same geometrical location (as defined in equation (A.5) below) would provide us with the amount of superheat ΔT_{Boil} and hence potential regions of flow boiling within the CFD model.

$$\Delta T_{Boil} = \max(0, (T - T_{sat})) \tag{A.5}$$

Variable Diesel Liquid Properties

The most detailed and comprehensive set of material properties for the light diesel fuel is provided in Multiphase Flow Dynamics 3 by N.I. Kolev [4].
In this study, the diesel fuel is assumed to be the light diesel with molecular weight of 170 kg/mol.

$$M = 170 kg/mol \tag{A.6}$$

The variations of diesel liquid density ρ, thermal conductivity k, specific heat capacity C_p and kinematic viscosity ν (in SI units) as functions of both temperature T and pressure p are given by the following seven equations [4].

$$\rho = \sum_{i=1}^{3} (\sum_{j=1}^{3} a_{ij} T^{j-1}) p^{i-1} \tag{A.7}$$

Where a_{ij} are the components of the matrix A shown below

$$A = \begin{bmatrix} 8.285974E+02 & 6.39930E-01 & -2.16000E-03 \\ 8.65679E-07 & -5.93672E-09 & 1.56678E-11 \\ -7.59052E-16 & 8.99915E-18 & -2.77890E-20 \end{bmatrix}$$
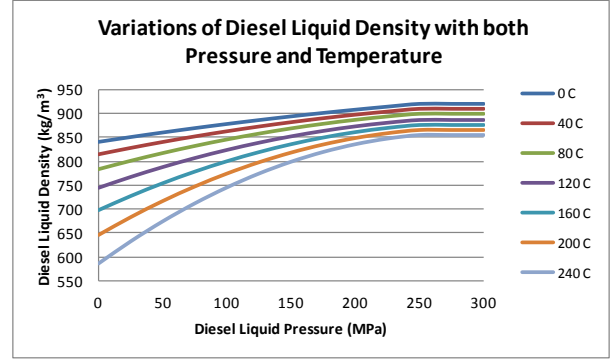$$\tag{A.8}$$

Figure A3. Variations of diesel liquid density with both pressure and temperature.

$$k = \sum_{i=1}^{3} (\sum_{j=1}^{3} b_{ij} T^{j-1}) p^{i-1} \tag{A.9}$$

Where b_{ij} are the components of the matrix B shown below

$$B = \begin{bmatrix} 1.39240E-01 & 3.78253E-05 & -2.89732E-07 \\ 6.27425E-11 & 6.08052E-13 & 3.64777E-16 \\ -1.38756E-19 & -2.57608E-22 & -2.70893E-24 \end{bmatrix}$$
$$\tag{A.10}$$

The density and thermal conductivity equations (A.7), (A.8), (A.9) and (A.10) are valid for the pressure range from 0 to 250MPa and the temperature range from 0 to 400°C. Although local pressure and temperature values encountered in this study are not outside the above ranges, Figs. A3 and A4 provide the variations of these properties up to 300MPa as given within GFS and based on the assumption that at any given temperature, there is no further variation for each property with respect to pressure for values between 250 and 300MPa. Similarly at any given pressure, no further variation is assumed for each property with respect to temperature for temperature values outside 0 to 400°C range.
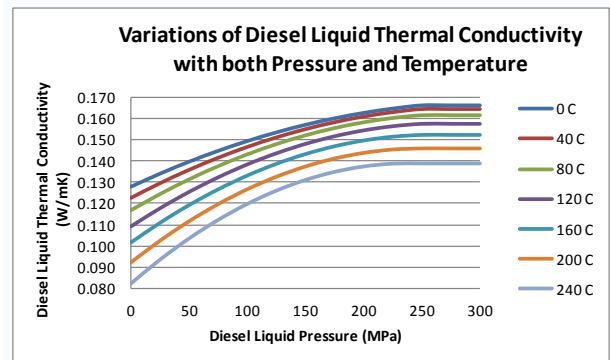

Figure A4. Variations of diesel liquid thermal conductivity with both pressure and temperature.

$$C_p = \sum_{i=1}^{5}(\sum_{j=1}^{3}d_{ij}T^{j-1})(\frac{p}{10^5})^{i-1} \qquad (A.11)$$

Where d_{ij} are the components of the matrix D shown below

$$D = \begin{bmatrix} -9.771619E+02 & 1.40251E+01 & -1.37400E-02 \\ 2.22361E-04 & -1.62143E-04 & 2.23214E-09 \\ -1.96181E-09 & 2.03748E-07 & -1.78571E-14 \\ 4.15000E-14 & -7.54100E-11 & 4.03897E-28 \\ -3.48714E-18 & 1.00688E-14 & -1.47911E-31 \end{bmatrix}$$
$$(A.12)$$

$$\log_{10}(10^6 \upsilon) = 8.67271 - 0.04287T + 5.31710*10^{-5}T^2$$
$$+ (0.00538 - 2.78208*10^{-5}T + 3.74529*10^{-8}T^2)(\frac{p}{10^5})$$
$$(A.13)$$

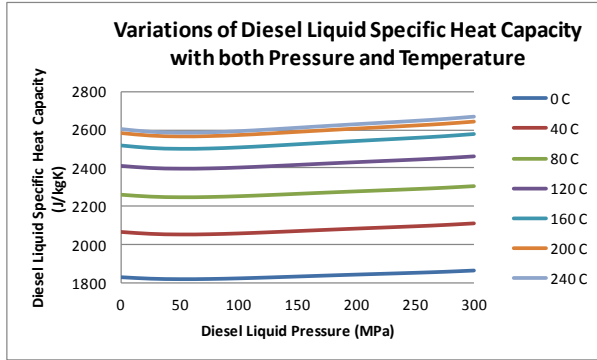**Variations of Diesel Liquid Specific Heat Capacity with both Pressure and Temperature**

Figure A5. Variations of diesel liquid specific heat capacity with both pressure and temperature.

The specific heat capacity and kinematic viscosity equations (A.6), (A.7) and (A.8) are however valid for the full pressure range from 0 to 300MPa while the validity of their temperature range is from 0 to 400°C and 0 to 120°C respectively. Figs. A5 and A6 show the variations of these properties with respect to both temperature and pressure values of up to 300MPa. However once again at any given pressure, GFS assumes no further variation for each property with respect to temperature for temperature values outside their corresponding range of validity. In the context of the current study, the main significance of this assumption is only on the kinematic viscosity results where local temperatures in excess of 120°C (but less than 400°C) were predicted within the flow field.
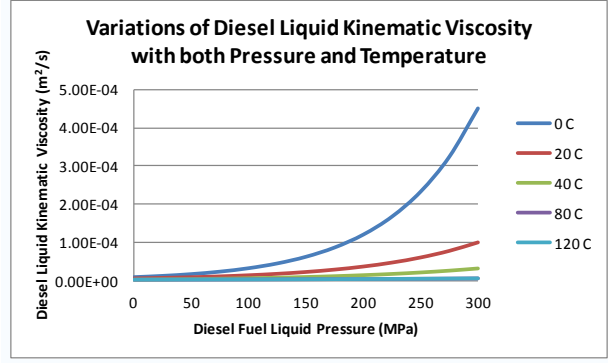
Variations of Diesel Liquid Kinematic Viscosity with both Pressure and Temperature

Figure A6. Variations of diesel liquid kinematic viscosity with both pressure and temperature.

Additionally Kolev [4] also provides the variations of the derivative of specific enthalpy with respect to pressure at constant temperature, which is then used to derive the overall variations of enthalpy again as functions of both temperature and pressure as shown below.

$$(\frac{\partial h}{\partial p})_T = \sum_{i=1}^{3}(\sum_{j=1}^{3}c_{ij}T^{j-1})p^{i-1} \qquad (A.14)$$

Where c_{ij} are the components of the matrix C shown below

$$C = \begin{bmatrix} 4.04000E-03 & -1.54245E-05 & 2.20238E-08 \\ -7.34229E-11 & 4.84276E-13 & -8.79805E-16 \\ 2.23591E-19 & -1.60598E-21 & 3.17966E-24 \end{bmatrix}$$
$$(A.15)$$

Based on equations (A.11), (A.12), (A.14) and (A.15) and using the same reference temperature and pressure as that provided by Kolev [4], and shown below, one can derive the variations of enthalpy and entropy as functions of pressure and temperature assuming reference enthalpy and entropy of zero at the following reference pressure and temperatures.

$$p_{ref} = 101325Pa \qquad (A.16)$$

$$T_{ref} = 288.15K \qquad (A.17)$$

$$h = (-144.2589124 + 1.42408*10^{-3}p$$
$$-3.46468*10^{-12}p^2 + 8.27879*10^{-21}p^3) +$$
$$(-1.91102*10^5 - 977.161T +$$
$$7.01247T^2 - 4.58000*10^{-3}T^3)$$
$$(A.18)$$

$$s = (-7.90013 * 10^{-2} + 7.80789 * 10^{-7} p$$
$$- 1.09258 * 10^{-14} p^2 + 2.78281 * 10^{-23} p^3) +$$
$$(2.04656 * 10^3 - 976.724 \ln T$$
$$+ 14.0737 T - 6.86780 * 10^{-3} T^2)$$

$$(A.19)$$